CrossMark

ORIGINAL PAPER

Atomic Structure of Heterophase Junction from Theoretical Prediction

Sheng-Cai Zhu[1] · Shu-Hui Guan[1] · Wei-Na Zhao[1] · Zhi-Pan Liu[1]

Abstract The heterophase junction is of great importance in photocatalysis and many other applications. The mechanical, optical and electrical properties of metrical are sensitive to the atomic structure of the heterophase junction. To date, the determination of these structures at the atomic level has been of great challenge for both experiment and theory. In this focused review, we introduce the recently developed theoretical methods based on stochastic surface walking method, which in combination with finite strain theory and first principles calculations can be utilized for identifying the homogeneous phase transition pathway and characterizing the atomic structure at the phase junction. The orientation relation and the atomic habit plane obtained from theory provide the key information for constructing the coherent phase junction. We then discuss the application of the method in two example systems in the context of latest experimental findings, namely TiO_2-B/anatase and anatase/rutile heterophase junction that are of wide application in photocatalysis. Using these examples, the merits and deficiencies of the current theoretical tools are illustrated. New theoretical approaches are called for towards the simulation of the solid-to-solid phase transition in real time and the characterization of heterostructure junction in general.

✉ Zhi-Pan Liu
  zpliu@fudan.edu.cn

[1] Collaborative Innovation Center of Chemistry for Energy Material, Shanghai Key Laboratory of Molecular Catalysis and Innovative Materials, Key Laboratory of Computational Physical Science (Ministry of Education), Department of Chemistry, Fudan University, Shanghai 200433, China

1 Introduction

Heterogeneous catalysts often contain multiple components with various kinds of junctions. In electro- and photo catalysis, it is generally accepted that the catalytic performance may be dramatically improved by compiling heterostructures with different Fermi levels [1–5], where the junction can tune the electron migration behavior [6–8]. Obviously, these junctions not only are of mechanical importance to glue material together but also may play important role in catalytic conversion. However, due to the complex nature of the reaction at the solid–solid interface, it is often not possible to answer even simplest question, "how do two solid materials join together", which requires the knowledge on the microscopic structure of the interface. This review focuses on some recent theoretical progress to determine the structure and understand the physiochemical properties of the crystal-to-crystal heterophase junction via the solid–solid phase transition, one important class of multicomponent junction in photocatalysis.

Semiconducting photocatalysts as represented by TiO_2 have been extensively investigated in the past several decades [9–12]. Intriguing phenomena related to the mixed TiO_2 oxides were observed by many research groups. The anatase/rutile bilayer film synthesized by Kawahara et al. [1] exhibit higher photocatalytic activity for CH_3CHO oxidation relative to the individual components. Zhang et al. [13] also found that the anatase/rutile mixed TiO_2 synthesized by impregnation are four times more active than pure rutile for water photocatalytic splitting. Similarly, TiO_2-B/anatase mixed oxide

synthesized by wet chemical condition also boosts the photoactivity in degradation of dye. [14] While mixed phase TiO$_2$ oxides are practically utilized and are generally more active than single-crystal oxide in photocatalysis, it is not until recent years that the presence of phase junctions is recognized as a main cause.

The phase junction not only can improve the ability of solar energy harvesting but also facilitate the subsequent chemical reactions, e.g. those related to pollutant decomposition. Because the structurally disordered interface with the stacking faults or dislocations can trap photo-generated charges [14] and not beneficial in photocatalysis, it is a general concern on how to synthesize high quality, structurally ordered interface at the atomic level. Experimentally, the heterostructure materials can be prepared via different approaches, including the partial solid-to-solid phase transition, the colloidal seed-growth [15–18] and chemical vapor deposition second-growth [19, 20]. Among them, the partial solid-to-solid phase is technically simple and widely used for synthesizing mixed phase photocatalysts, but it is also more difficult to control the structure of the junction.

For its importance, intensive researches have been devoted to resolve the microscopic structure of the heterophase junction and to understand the solid–solid phase transition mechanism in the past decades. New experimental techniques have been applied to characterize the interface structure, including in situ heat TEM [21–24], in situ X-ray diffraction [25–27] and in situ Raman spectrum [28, 29]. In addition, recent years have also seen the efforts using computational simulations to optimize the solid–solid interface. From a theoretical point of view, the main bottleneck in simulation is to capture the atomic movement at the interface, where the reaction barrier is generally too high to overcome by using conventional molecular dynamics [30–32] method. The simulation time needs to be extremely long in order to identify the most stable interface. To enhance the structure search ability, new theoretical methods, such as basin-hopping method [33], genetic algorithm [34], metadynamics [35–37], stochastic surface walking (SSW) method [38–40] have been developed and utilized to study the interfacial structure and the solid phase transition mechanism.

The purpose of the article is to provide our latest theoretical thinking in this emerging field and motivate further scientific research. We will introduce our recently developed SSW pathway sampling method for solid-to-solid phase transition and present the procedure for finding stable interface structures. Two TiO$_2$ examples analyzed using the current theoretical methods are provided, where the structures of heterophase junctions have been studied extensively in literatures. These systems are important in photocatalysis and have been extensively studied in experiment. The theoretical results are thus discussed in the context with experimental findings.

2 Theoretical Methods for Identifying Coherent Heterophase Junction

2.1 SSW Pathway Sampling for Solid–Solid Phase Transition

SSW method is targeted for automated potential energy surface (PES) exploration of many-atom system [38–40]. It can be utilized to identify unexpected new structures, including clusters and crystals, and at the mean time to collect the reaction pathways leading to them. This is attributed to the fact that SSW PES searching involves generally small displacement on atoms, and thus the pathway information is maintained from one minimum to another. The method is originally developed for aperiodic systems, i.e. molecules and clusters, and is recently extended to crystal systems by coupling the degrees of freedom of lattice with those of atom. The method has been successfully utilized for predicting the structure of finite clusters with complex PES, such as C$_{100}$ fullerene, and the detail of the algorithm can be found previously. [38–40] Here we briefly outline the central idea of the SSW method and an illustration of the SSW method in 1-D PES is shown in Fig. 1a.

The SSW algorithm [38–40] features with an automated climbing mechanism to manipulate a structure configuration from a minimum to a high energy configuration along one random direction. The idea of the climbing is inherited
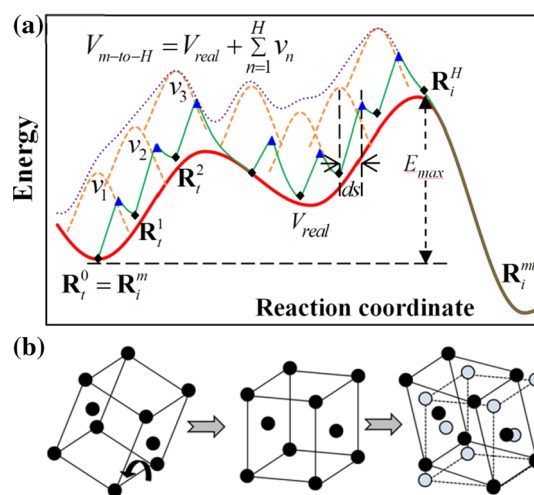

Fig. 1 a The illustration of the SSW method in 1-D PES (Copyright from RSC [40]); **b** The illustration of homogenous crystal phase transition. The phase transition can be divided into two steps: (i) the lattice rotation; and (ii) the lattice deformation

from the bias-potential driven constrained-Broyden-dimer (BP-CBD) method for TS location [41], which is designed to enable the method to overcome the high barrier encountered in chemical reactions. Specifically, in one particular SSW step (Fig. 1a), labeled as i, a modified PES V_{m-to-n} (n is the index of the bias potential, $n = 1,2,\cdots H$), as shown in Eq. 1, is utilized for moving from the current minimum, $\mathbf{R}_i^m$ to a high energy configuration $\mathbf{R}_i^H$ (the climbing), in which a series of bias Gaussian potential v_n is added one by one consecutively along the direction $\mathbf{N}_i^n$.

$$
\begin{aligned}
V_{m-to-H} &= V_{real} + \sum_{n=1}^{H} v_n = V_{real} + \sum_{n=1}^{H} w_n \\
&\times \exp\left[-\left((\mathbf{R}^t - \mathbf{R}_t^{n-1}) \cdot N_i^{n-1}\right)^2 \middle/ \left(2 \times ds^2\right)\right]
\end{aligned}
\tag{1}
$$

where $\mathbf{R}$ is the coordination vector of the structure and V_{real} represents the unmodified PES; $\mathbf{R}_t^n$ are the nth local minima along the movement trajectory on the modified PES that is created after adding n Gaussian functions (see Fig. 1a). The Gaussian function is controlled by its height w and its width ds, and is always added along one particular walking direction as defined by $\mathbf{N}^n$. Once the $\mathbf{R}_i^H$ is reached, all bias potential are removed and the local optimization is performed to quench the structure to a new minimum.

The SSW method can also be utilized for reaction pathway sampling. Take the crystal phase transition as the example [40], the purpose of SSW crystal pathway sampling is to establish a one-to-one correspondence for lattice (L_t, t = a, b, c, being three lattice vectors) and atom (q_i, i = 1,…3N, N is the number of atom in cell) from one phase to another (see Fig. 1b). The one-to-one correspondence of two phases (P1 and P2) can be simply summarized as the orientation relation (OR), which include a pair of parallel crystallography planes $(hkl)_{P1}//(hkl)_{P2}$ that attach with each other at the junction and a pair of parallel directions $[uvw]_{P1}//[uvw]_{P2}$. The lattice here does not necessarily refer to the conventional Bravais lattice but can be any possible set of lattice that describe the same crystal phase. Using such a pair of coordinates, $Q_{IS}(L,q)$ and $Q_{FS}(L,q)$ (IS and FS are the initial and the final states), it is then possible to utilize double-ended transition state (TS) searching method to identify the reaction pathway and the TS. This approach for studying solid phase transition is different from the traditional Landau-type theory where the lattice correspondence needs to be assumed. Three steps are involved for finding the lowest energy pathway, as described below briefly.

2.1.1 Pathway Collection

In SSW pathway sampling, firstly, we start from one single phase (starting phase), and utilize the SSW method to explore all the likely phases nearby the phase. A structure selection module is utilized to decide whether to accept/refuse once a

new minimum is reached. If the new phase different from the starting phase is identified by the SSW crystal method [40], we record/output the IS (i.e. starting phase) and the FS (a new phase) of the current SSW step. Then, the program will return back to the IS by rejecting the new minimum to continue the phase exploration; On the other hand, if the new minimum identified by SSW is still the starting phase (e.g. the same symmetry but a permutation isomer with varied lattice), the program will accept the new isomeric phase and start the phase exploration from this phase. We repeat this procedure until a certain number of IS/FS pairs are reached.

2.1.2 Pathway Screening

Secondly, we utilize the variable-cell double-ended surface walking (DESW) method [42] to establish the pseudopathway connecting IS to FS for all IS/FS pairs [41, 43]. The approximate barrier is obtained according to DESW pseudopathway, where the maximum energy point along the pathway is generally a good estimate for the true TS [42]. By sorting the approximate barrier height, we can obtain the candidates for lowest energy pathways.

2.1.3 Lowest Energy Pathway Determination

Thirdly, the candidate lowest energy pathways are selected to locate exactly the *true* TS by using DESW TS-search method [42]. By sorting the exact barrier calculated, the energy difference between the TS and the IS, the lowest energy pathways can be finally obtained. All the lowest energy pathways will be further confirmed by extrapolating TS towards IS and FS, and the TSs need to be validated by phonon spectrum calculation, showing one and only one imaginary mode.

2.2 The Orientation Relation and Coherent Interface

The lowest energy pathways determine the lattice and atom correspondence between two connecting phases. In order to identify the coherent interface between two phases, we can utilize the finite strain theory to analyze the strain for different crystallography plane pairs. Once several low strain candidate plane pairs are obtained, we further use the first principles calculations to build the interface and compute the interfacial energy. This procedure is outlined below in detail.

2.2.1 Step1: Determine Strain Invariant Planes

With the lattice correspondence between two crystals, we can first use the classical phenomenological theory of martensitic crystallography (PTMC) [44–50] that is based on finite strain theory to determine the invariant line strain, the possible habit planes and ORs.

2.2.1.1 Determine the Principal Axes of the Phase Transformation Let define two lattices as $\mathbf{T}$ and $\mathbf{M}$, both (3×3) matrix of lattice (see Fig. 1b). A deformation gradient $\mathbf{F}$ matrix transforms an initial lattice $\mathbf{T}$ to a final lattice $\mathbf{M}$, as

$$\mathbf{FT} = \mathbf{RBT} = \mathbf{M} \tag{2}$$

$$\mathbf{F} = \mathbf{RB} \tag{3}$$

where $\mathbf{R}$ is a rigid-body rotation matrix and $\mathbf{B}$ is a lattice deformation matrix, representing the generalized Bain deformation. In PTMC, $\mathbf{F}$ is also known as a homogeneous *invariant line strain*.

The Gauchy-Green deformation tensor is

$$\mathbf{C} = \mathbf{F^T F} = \left(\mathbf{T^T}\right)^{-1}\mathbf{M^T M T}^{-1} \tag{4}$$

$\mathbf{C}$ is rotational invariant. The principal axes are the eigenvectors ($\mathbf{e_i}$, i = 1, 2, 3) of the Gauchy-Green deformation tensor

$$\mathbf{Ce_i} = \mathbf{l_i e_i} \tag{5}$$

The strain energy of the lattice deformation is defined the sum of three eigenvalues, $\mathbf{l_i}$

$$I = \text{tr}(\mathbf{F^T F}) = \mathbf{l_1} + \mathbf{l_2} + \mathbf{l_3} \tag{6}$$

Similarly, for the interface, a two-dimensional problem, we can define the strain energy as

$$S = \mathbf{l_1} + \mathbf{l_2} \tag{7}$$

where $\mathbf{l_1}$ and $\mathbf{l_2}$ are the eigenvalues measuring the strain along the principal axis of the interfacial plane.

2.2.1.2 Determine the Strain Invariant Lines (SIL) and Strain Invariant Planes (SIP) For Martensitic phase transition, three eigenvalues of matrix $\mathbf{C}$ could not be all larger than one or all smaller than 1 and in general $\mathbf{l_2}$ should be quite close to unity:

$$\mathbf{l_1} < 1; \mathbf{l_2} > 1; \mathbf{l_3} > 1; \quad \text{or} \quad \mathbf{l_1} < 1; \mathbf{l_2} < 1; \mathbf{l_3} > 1 \tag{8}$$
$$(\mathbf{l_3} > \mathbf{l_2} > \mathbf{l_1})$$

Using three eigenvectors $\mathbf{e}$ as the basis, we need to determine the strain invariant lines on a corn surrounding the maximum or the smallest $\mathbf{e_i}$. This is equivalent to find the fractional coordinate (a, b, c) satisfying the following two equations.

$$a^2 + b^2 + c^2 = 1 \tag{9}$$

$$a^2\mathbf{l_1} + b^2\mathbf{l_2} + c^2\mathbf{l_3} = 1 \tag{10}$$

While there are in principle infinite number of solutions for (a, b, c), the problem can be simplified by identifying the strain invariant lines on the plane defined by the largest

and the smallest eigenvectors, $\mathbf{e}_1$ and $\mathbf{e}_3$., i.e. by setting $b = 0$. These strain invariant lines can thus be solved as

$$sil_1 = a\mathbf{e_1} + c\mathbf{e_3} \quad \text{and} \quad sil_2 = a\mathbf{e_1} - c\mathbf{e_3} \tag{11}$$

Using a *sil* vector and another untitled line, e.g. the principal axes $\mathbf{e}$ normal to *sil*, it is possible to construct the so-called strain invariant (minimum) plane, the habit plane. All lines on habit plane are unrotated, which should contain a strain invariant line and also an untitled line. These lines and their angle are unchanged under the rigid-body rotation and the lattice deformation. The habit plane normal *sip*, a unit vector, can be solved using

$$sip_k = sil_i \times \mathbf{e_j} \tag{12}$$

$$\mathbf{F}sip_k = \mathbf{RB}sip_k = sip_k \tag{13}$$

2.2.2 Step 2: Determine the Crystal Planes with Minimum Strain and Minimum Atomic Movement

The sip_i above considers only the lattice strain between two connecting phases. In order to identify the most likely crystallography planes for the phase junction, we need to go beyond PTMC by taking into account the magnitude of atomic movement in the phase transition. For diffusionless Martensitic phase transition, it is important that the atoms at the phase junction are closely matched and thus the atomic displacement needs to be as small as possible from one phase to another.

Based on the atom correspondence from the pathway, we can search for the crystal plane with minimum strain and minimum atomic movement.

a. The minimum strain condition is first utilized to screen the crystal Miller planes by minimizing the dihedral angle between the possible crystal plane ((hkl) with h, k, l being integer number) and the sip_i..

b. The atomic movement can be calculated by summing the displacement of each atom from initial to the final phase while projecting out those due to rigid-body rotation. The atomic movement is composed of two types of movement, parallel to the crystal plane (hkl) and perpendicular to the plane. For Martensitic phase transition, the phase transition is achieved often via slipping or twinning and thus the atomic movement needs to be dominated by those parallel to the habit plane.

2.2.3 Step 3: Identify the Atomic Habit Plane (Interface)

Finally, we utilize the determined possible atomic habit planes to establish the interface between two phases. With

the biphase lattice structure established, first principles geometry optimization calculations are performed to relax the interface and the interfacial energy γ_{int} can be computed using the following equation,

$$\gamma_{int} = [E(\text{biphase}) - \Sigma_i n_i E_i(\text{pure phase})]/2A \qquad (14)$$

where E (biphase) is the total energy of the biphase crystal, E_i(pure phase) is the energy of pure phase, n_i is number of formula units of the different phase components in the biphase and A is the surface area of the interface. Obviously, the lower γ_{int} (in general <1 J/m^2) is, the more stable the interface will be. An atomic habit plane should exhibit a coherent interface between two phases, i.e. with the lowest interfacial energy.

3 Examples of Phase Junction

3.1 TiO$_2$-B/Anatase Interface

Titania is one of the most widely used photocatalysts. It has a number of phases, including rutile (P4$_2$/mnm, #136), anatase (I4$_1$/amd, #141), brookite (Pbca, #61) and TiO$_2$-B (C2/M, #12) crystal phases. TiO$_2$-B is a metastable phase and can transit to anatase by heating. This enables the fabrication of TiO$_2$-B/anatase phase junction by partial phase transition at the high temperature. As the photocatalyst for water splitting and pollutant control, TiO$_2$-B based systems have been studied by many research groups. [7, 51–57] It was reported that the presence of TiO$_2$-B/anatase phase junction in the nanofiber can dramatically increase the photoactivity of the catalyst. [54] For example, a bi-crystal mixture phase TiO$_2$ nanoparticles containing major anatase and minor TiO$_2$-B exhibits higher photoactivity than the commercial P25 for the degradation of sulforhodamine B. [14] The performance of water splitting on Pt/mesoporous TiO$_2$-B/anatase composite is much better than both bare and Pt-loaded P25. [53]

The mechanism and the OR of TiO$_2$-B to anatase phase transition were debated in literatures [7, 14, 51–57]. Two representative ORs suggested recently based on HRTEM observations are [010]$_A$//[010]$_B$, [001]$_A$//[100]$_B$ reported by Li et al. [52] ([uvw] represents the real space vector), and [010]$_A$//[010]$_B$ (001)$_A$//(100)$_B$ suggested by Yang et al. [14] (see Fig. 2). However, the atomic model for the interface constructed according to these assignments cannot maintain the octahedron unit of Ti ions with either too close contact between Ti ions or O ions and thus the proposed interface atomic structure are energetically unfavorable. Apparently, this is not consistent with the high photoactivity of TiO$_2$-B/anatase biphase crystal.

Recently, we utilized SSW pathway sampling to the lowest pathway from TiO$_2$-B to anatase [58]. As shown in Fig. 3, the lowest energy pathway is a one-step reaction with a barrier of only 0.12 eV per TiO$_2$ unit. The other transition pathways leaving TiO$_2$-B phase are energetically much higher. It can be identified that the atomic habit planes of the phase transition (blue dotted line, Fig. 3) is TiO$_2$-B (-201) and anatase (103). The OR of TiO$_2$-B/anatase transition is thus written as (-201)$_B$//(103)$_A$, [010]$_B$//[010]$_A$. According to the OR, the phase junction can be constructed by attaching (-201)$_B$ with (103)$_A$, also shown in Fig. 3.

The theoretical OR for the phase transition was proved by HRTEM observation of the TiO$_2$-B/anatase bicrystalline material. [58, 59] By rotating the zone axis in HRTEM, we have measured the dihedral angles for a set of surface planes, which can be compared with the theoretical predicted values (Table 1). The agreement between theory and experiment is good, indicating that the lowest energy pathway from SSW pathway sampling is followed in the phase transition. The phase transition is proposed to initiate from (-201)$_B$ surface and propagate layer-by-layer along the [-10-2]$_B$ direction into the bulk. The calculated barrier for forming the first layer anatase is 0.49 eV per $p(1\times1)$ cell from DFT and the overall barrier to form two layers of anatase is slightly higher, being 0.58 eV. Based on the results, it was concluded that the TiO$_2$-B/anatase phase junction can be regarded as a perfect phase junction that lacks of the common stacking faults or dislocation defects, those otherwise are commonly present during the growth and packing of crystals [60].

Figure 4 shows the calculated electronic structure of a mixed phase TiO$_2$-B/anatase in a superlattice constructed using the OR presented above, which exhibits spatially separated valence band maximum (VMB) and conduction band minimum (CBM). The VBM where the photogenerated hole resides is dominantly accumulated on the TiO$_2$-B side, while the CBM where the photogenerated electron stays is mainly populated on the anatase side. The presence of the ordered phase junction can affect largely the photogenerated electron/hole migration in the catalysts: the hole will prefer TiO$_2$-B phase while the electron goes oppositely towards anatase from the band alignment in Fig. 4 (middle). The knowledge on the phase junction helps to understand the experimental finding that the photoactivity of the mixed phase nanofibers is superior to the pure phase, as also shown in Fig. 4 (right). Apparently, the structurally ordered interface between two phases can significantly reduce the possibility of the electron–hole pair recombination and thus increase the quantum efficiency of photocatalysts.

3.2 Anatase/Rutile

Anatase and rutile are two most common phases of TiO$_2$ and widely utilized as photocatalysts. Anatase is more
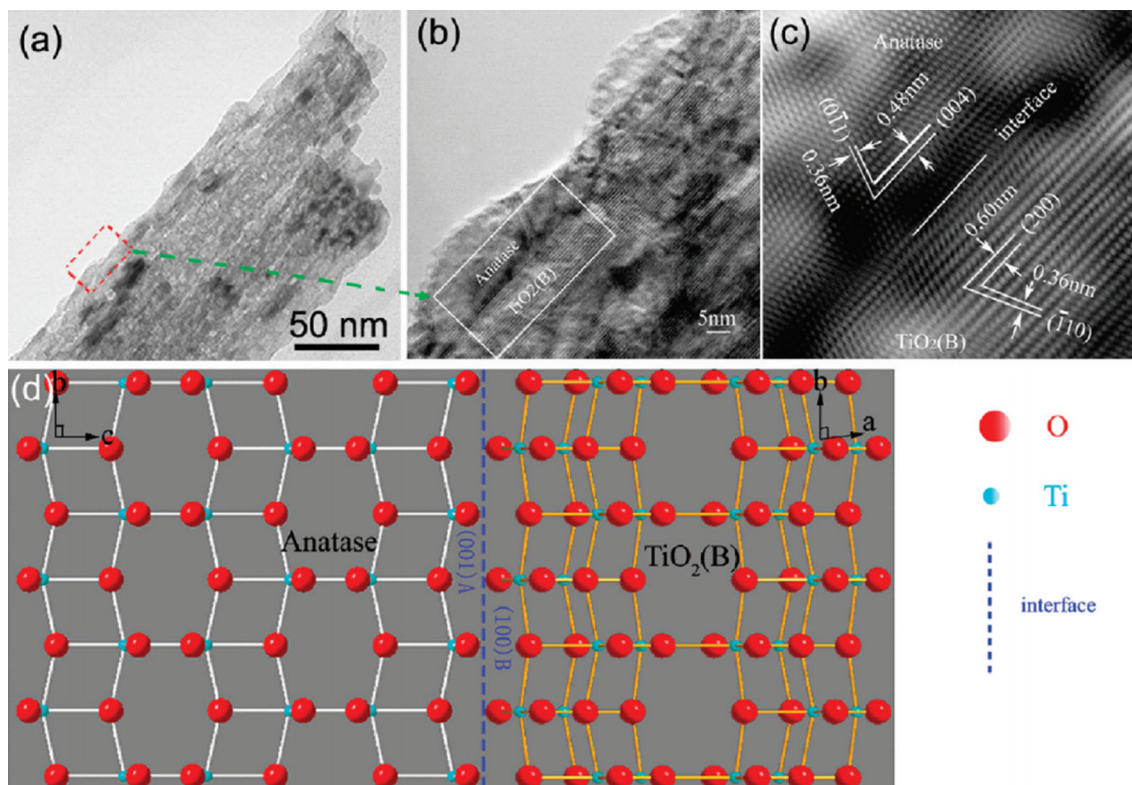
Fig. 2 Images of the TiO_2-B/anatase: **a** TEM images, **b** HRTEM image, **c** inverse fast Fourier transition (IFFT) image of the selected area, and **d** schematic atomic arrangement of the interface TiO_2-B/anatase (Copyright from ACS [14])

stable as nanoparticles due to the favored surface energies, while rutile is more stable as the bulk phase. The conversion of the two phases has been widely exploited in experiment for synthesizing different morphology TiO_2 [61] and of great importance in application, in particular, for the photocatalytic water splitting [62–66]. It is known since 1990s that the anatase/rutile mixed phase nanocrystal samples as represented by the commercial P25 catalysts outperform the individual polymorphs.

The phase transition kinetics from anatase to rutile has been studied in detail in experiment by Banfield group [6, 67–71] and Li group [72, 73]. Although different kinetic model were proposed, it is the consensus that the phase transition initiates from anatase particles at the temperature of ~ 835 K. However, the atomic-level mechanism remains uncertain. A number of possible mechanisms have been proposed in literatures, differing by the intermediate state during phase transition, via e.g. brookite [60, 67], TiO_2-II [74–78], amorphous phase [79], or without intermediate [80]. The HRTEM image of anatase/rutile junction fabricated by the second growth approach was reported (see Fig. 5a), which showed that the contact area between rutile and anatase is limited (non-wetting behavior), indicating a large strain developed at the interface. [13] The

phase junction could also act as the anchoring site for the growth of metal nanoparticles [81] (see Fig. 5b).

Theoretically, several groups have constructed the structure of the direct anatase/rutile phase junction based on molecular dynamics simulations or straightforward geometry optimization. Ju et al. [4] utilized $(101)_A$ and $(111)_R$ as the junction planes, where anatase (101) p(1 × 3) (5.44 Å × 11.3 Å with $\phi = 110.3°$) matches with rutile (111) p(1 × 2) (5.46 Å × 10.9 Å with $\phi = 107°$). Xia et al. [82] considered $(101)_R$ and $(001)_A$ pair as the junction planes to build the biphase crystal and used the model to explain the preferential heating of anatase phase. Using force field calculations, Deskins et al. [83] identified several interface structure models that are energetically likely, including $(110)_R//(101)_A$ and $(100)_R//(100)_A$. But, these optimized structures are generally rather disordered at the interfacial layers (~ 4 Å) due to the large strain at the junction, which implies that the electron/hole transport through the interface is frustrated.

Using the SSW pathway sampling method, we recently identified the lowest phase transition pathway between anatase and rutile crystals (using 12-atom supercell). [40] Unexpectedly, a high-pressure phase TiO_2-II (α-PbO_2-like form) is found to be the intermediate between rutile and

Fig. 3 (*Top panel*) DFT lowest energy transition pathway from TiO$_2$-B to anatase bulk crystal (structures viewed down from *b* axis). The blue lines indicate the habit plane of the phase transition. (*Bottom panel*) The atomic structure of the TiO$_2$-B/anatase phase junction with OR (-201)$_B$//(103)$_A$; [010]$_B$//[010]$_A$ as predicted from theory. From left to the right are the top-views of (103)$_A$ and (-201)$_B$, and two side-views of the junction showing the (100)$_B$ together with (001)$_A$ (theoretical dihedral angle 11.0 degrees), and (010)$_B$//(010)$_A$. *Ti* grey balls, *O* red balls. (Copy right from ACS, Ref. [58])

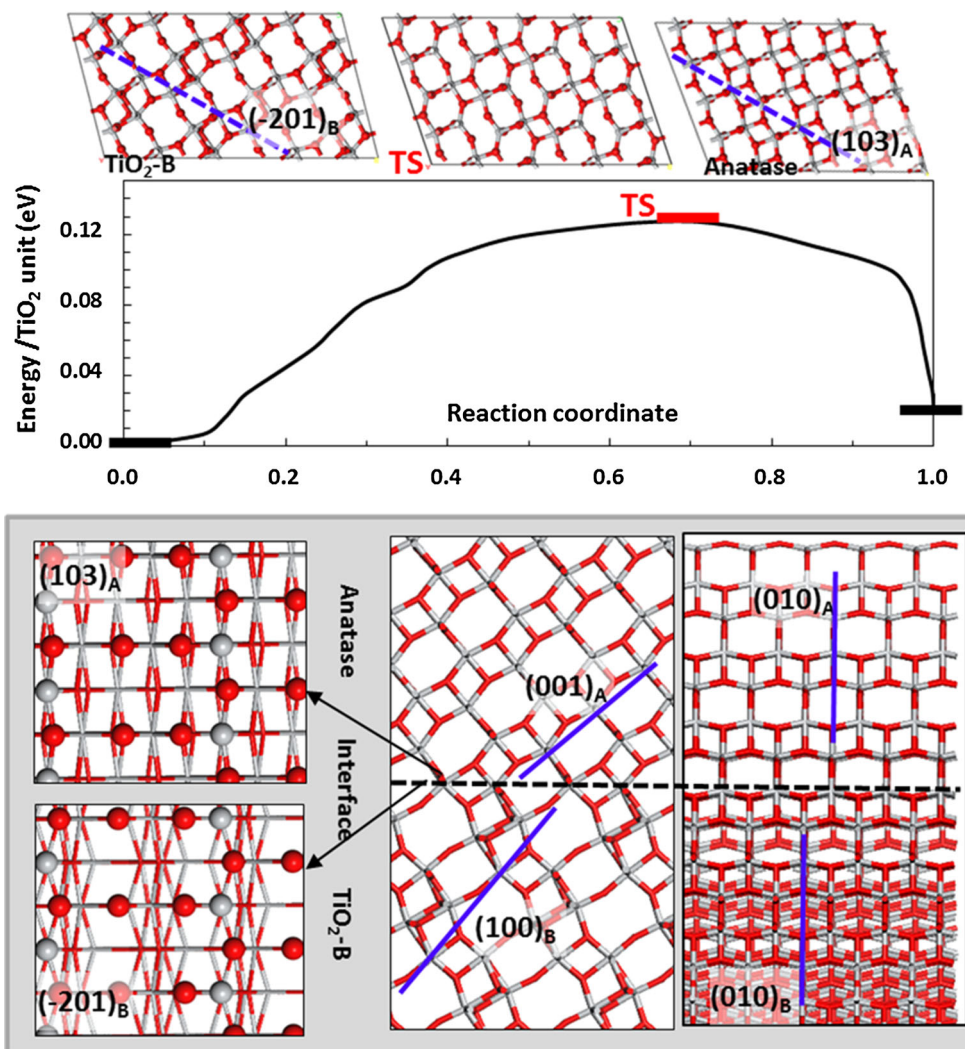**Table 1** The dihedral angles between the crystallographic planes of two phases measured by experiment and predicted by theory. [58]

TiO$_2$-B	Anatase	Experiment (±1°)	Theory (°)
(020)	(020)	0	0.0
(−201)	(103)	0	0.0
(−110)	(011)	6	5.3
(310)	(004)	48	47.0
(100)	(020)	90	90.0
(020)	(004)	90	90.0
(31–2)	(1-12)	179	179.3

anatase. The lowest energy pathway suggests a crystallographic correspondence between the three phases, i.e. rutile (101) plane being parallel with TiO$_2$-II (001), (101)$_R$//(001)$_{II}$, and anatase(112) being parallel with TiO$_2$-II (100), (100)$_{II}$//(112)$_A$. [40] This finding is consistent with known

experimental results on the appearance of TiO$_2$-II phase during the anatase to rutile transformation under high pressure synthetic conditions. [84]

Based on the knowledge from SSW sampling pathways, we selected anatase(112), TiO$_2$-II(100) and and TiO$_2$-II(001) rutile(101) as the main candidates for the interfacial planes constituting the phase junction, since these crystallography planes dominate the OR in the lowest energy pathways. In Table 2, we compared our junction models with previously studied models, both the direct two-phase junction and the indirect three-phase junction. The interfacial strain energy S and interfacial energy γ_{int} can be computed by using Eqs. 7 and 14 in the previous section, respectively. [85]

We found that the strain energy S for OR **I,** the direct interface (101)$_R$ and (112)$_A$ is among the smallest, i.e., 2.37, for the direct interface models (the equivalent density condition of two phases is enforced in searching for the best matched interface). More importantly, we found that
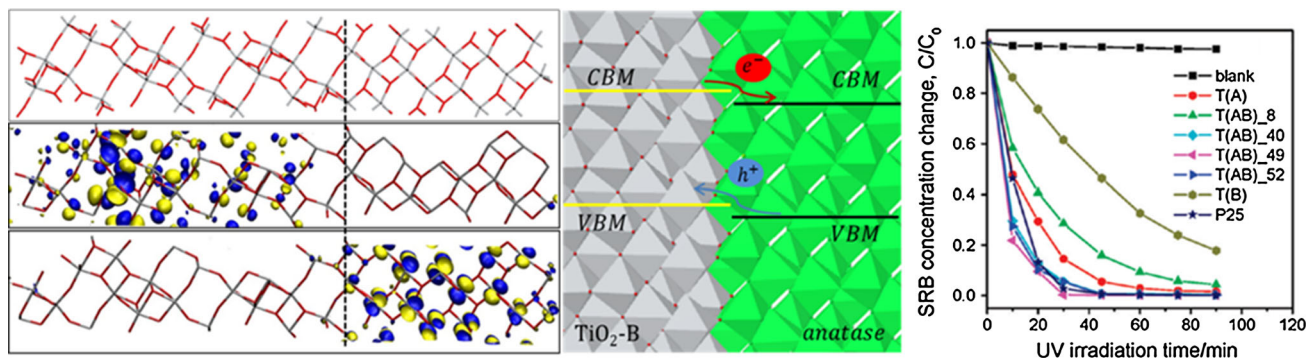
Fig. 4 The electronic structure of TiO$_2$-B/anatase and its photocatalytic activity. (*Left*) The structure and wave function of a superlattice biphase crystal, containing half–half TiO$_2$-B/anatase phases, showing the spatially well separated valence band maximum (*Left-middle*) and the conduction band minimum (*Left-bottom*). The dotted line indicates the interface. The isosurface density value of the plots is 0.02 e/bohr^3. (*Middle*) The scheme for the band alignment between TiO$_2$-B (*grey color*) and anatase (*green color*) at the phase junction. (Copy right from ACS, Ref. [58]) (*Right*) Photocatalytic decomposition of SRB with different fibril TiO$_2$ photocatalysts under UV irradiation (Copyright from ACS, Ref. [14]), showing the mixed TiO$_2$-B/anatase phase photocatalyst can be much more active than single phase photocatalysts
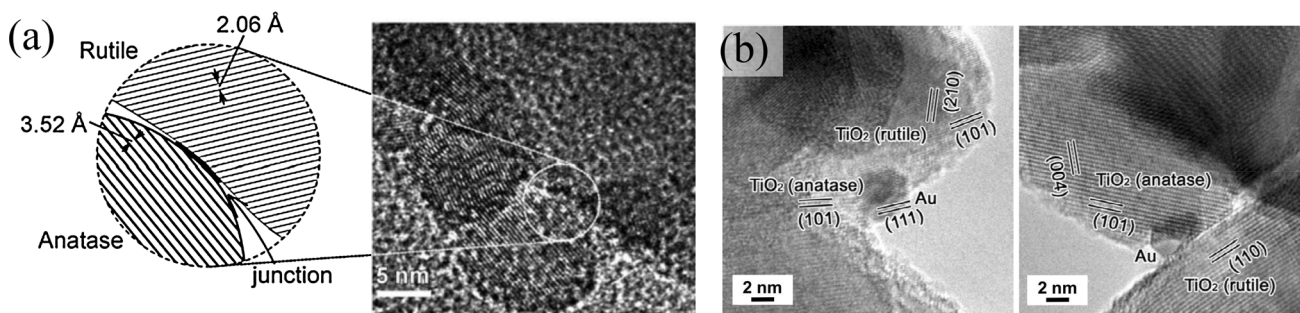

Fig. 5 HRTEM images of anatase/rutile interface from literatures. **a** The phase junction synthesized using second growth method (Copyright from Wiley [13]); **b** Au particles on anatase/rutile (P25) interface (Copyright from ACS [81])

by introducing the intermediate TiO$_2$-II phase, thus the indirect junction, the strain energy at the interface can be reduced down to 2.01 and 2.18 for rutile/TiO$_2$-II and anatase/TiO$_2$-II interface in OR **V** and **VI**, respectively. These OR pairs are indeed those obtained from lowest energy pathways in SSW pathway sampling. The procedure to construct these phase junction structures are illustrated in Fig. 6. Based on these biphase crystal models, the electron/hole migration behavior could then be investigated using electronic structure calculations, which could provide deeper understandings into the photocatalysis on multiple component materials.

Figure 7 shows the calculated electronic structure for the anatase/TiO$_2$-II and rutile/TiO$_2$-II superlattices, where the wave function at the CBM and VBM are plotted. For anatase/TiO$_2$-II, the VBM mainly locates at the TiO$_2$-II side around the lattice O sites, while the CBM is distributed at the anatase side around the lattice Ti sites. By contrast, for rutile/TiO$_2$-II, both VBM and CBM mainly locate in the rutile phase. These indicate that the anatase/TiO$_2$-II phase junction is more important for enhancing charge separation

in photocatalysis. Overall, the electronic structure of the phase junctions are sensitive to the local geometrical structure. In order to provide deep understanding for the photocatalytic activity of mixed phase catalysts, it is critical to determine the local interfacial structure and align the band levels between different phases.

4 Concluding Remarks

Solid-to-solid phase transition is an important phenomenon in nature and has been exploited in photocatalysis for synthesizing active photocatalysts. In the past years, thanks to the advance in theoretical methods, the understanding on the mechanism of phase transition has reached to the atomic level. The preceding sections serve to highlight the methodology development for characterizing the phase junction structure based on SSW pathway sampling method, the insights into the phase transition mechanism and the structure of the phase junction in two TiO$_2$ examples.

Table 2 Models for anatase–rutile phase junction, the computed strain energy S and the interfacial energies γ_{int}. The phase junction is constructed by joining two phases (P1 and P2) according to the OR. [86]

OR	P1		P2		S	γ_{int} (J/m²)
	a (Å)	b (Å)	a (Å)	b (Å)		
Direct model						
I	5.38	5.54	5.51	4.65	2.37	0.58
II	5.51	5.51	5.34	3.81	3.83	0.88#
III	5.34	3.81	4.65	4.65	2.49	/
IV	9.68	3.81	6.57	2.97	3.81	/
Indirect model						
V	5.51	4.65	5.59	4.60	2.01	0.01
VI	5.59	4.95	5.38	5.54	2.18	0.11
VII	5.59	6.76	5.38	5.54	2.57	/
VIII	5.38	5.54	5.59	4.60	2.35	/

* OR are as follows. **I** $(112)_A//(101)_R$, $[1\text{-}10]_A//[10\text{-}1]_R$; **II** $(111)_R//(101)_A$, $[01\text{-}1]_R//[010]_A$; **III** $(101)_A//(001)_R$, $[010]_A//[010]_R$; **IV** $(100)_A//(110)_R$, $[001]_A//[1\text{-}10]_R$; **V** $(101)_R//(001)_{II}$, $[10\text{-}1]_R//[100]_{II}$; **VI** $(100)_{II}//(112)_A$, $[010]_{II}//[1\text{-}10]_A$; **VII** $(101)_{II}//(112)_A$, $[10\text{-}1]_{II}//[1\text{-}10]_A$; **VIII** $(112)_A/(001)_{II}$, $[1\text{-}10]_A//[100]_{II}$

from Ref. [4]

The SSW pathway sampling for crystal can reveal the solid-to-solid transition pathways and thus provide important insights into the connectivity of the crystal phases on the PES. With the explicitly located TSs and computed energy barriers, it would be possible to utilize the conventional TS theory to understand the solid-to-solid phase transition mechanism. Three basic types of phase transition could be conceived from the pathways at the atomic level. For **Type-I,** the phase transition should propagate mainly along one and only one direction (e.g. defined by a habit plane). The phase transition is characterized by a single low energy pathway and a low energy interface. By this way, the formed phase junction can be atomically sharp, e.g. being built of two particular sets of epitaxial joined planes of two component phases. For **Type-II,** the phase transition propagates along more than one direction due to the presence of energy degenerate phase transition channels. For **Type-III,** the phase transition involves an intermediate phase and the transition propagates along more than one direction. In both **Type-II** and **Type-III** phase transition, the accumulated stress at the fronts of phase boundaries could yield large deformation at the phase junction and thus they are less likely to produce atomically sharp interface. As for the two examples discussed above, TiO$_2$-B/anatase belongs to **Type-I** phase junction and anatase/rutile belongs to the **Type-III** phase junction.

To date, the applications of SSW crystal pathway sampling are limited to the diffusionless, defect-free phase transition modeled by relatively small bulk unit cell, the results of which are the homogeneous phase transition pathways starting from a single crystal phase. However, the phase transition in reality is much more complex, involving possibly the seeding-growth, the anisotropic propagation, the defects, the dopant and complex reaction conditions (e.g. high pressure). In addition, other types of heterostructure junctions, e.g. those composing of more than one type of materials, are also not feasible within the current framework of the SSW crystal pathway sampling. The large-scale simulation using global optimization method can in principle to solve the structure of heterostructure junction containing multiple components. But, due to the complexity of PES for heterostructure systems, we expect that the automated brute-force global structure search based on quantum mechanics calculations is still far beyond reach even with the rapid increase of computational power. Instead, new indirect theoretical approaches, such as the method introduced here for gluing two phases together, would provide some practical solutions in the future.
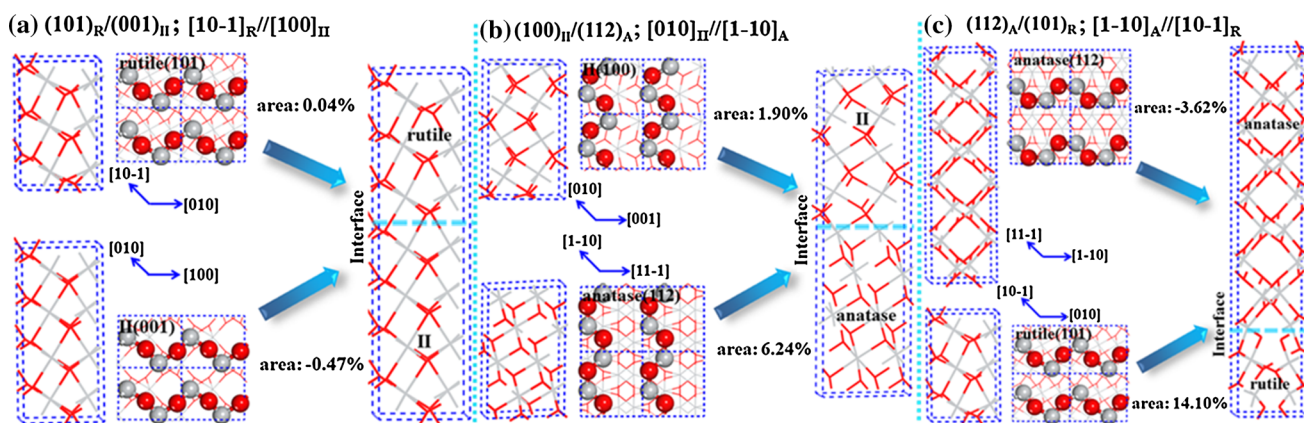

Fig. 6 Construction of biphase phase-junction using OR in Table 2. **a** Rutile/TiO$_2$-II (OR **V**) **b** TiO$_2$-II/anatase (OR **VI**) and **c** anatase/rutile (OR **I**), *Ti grey, O red*. [86]

Fig. 7 The structure and wave function of a superlattice biphase crystal, (**a**) and (**b**) containing 12anatase/2II phases, showing the spatially well separated VBM and CBM, (**c**) and (**d**) containing 4rutile/1II phases, showing VBM and CBM mainly locate in the rutile phase. The dotted line indicates the interface. *Grey* Ti atoms, *Red* O The isosurface value is set as ± 0.14 e/Å^3. (Copyright from Ref. [86])
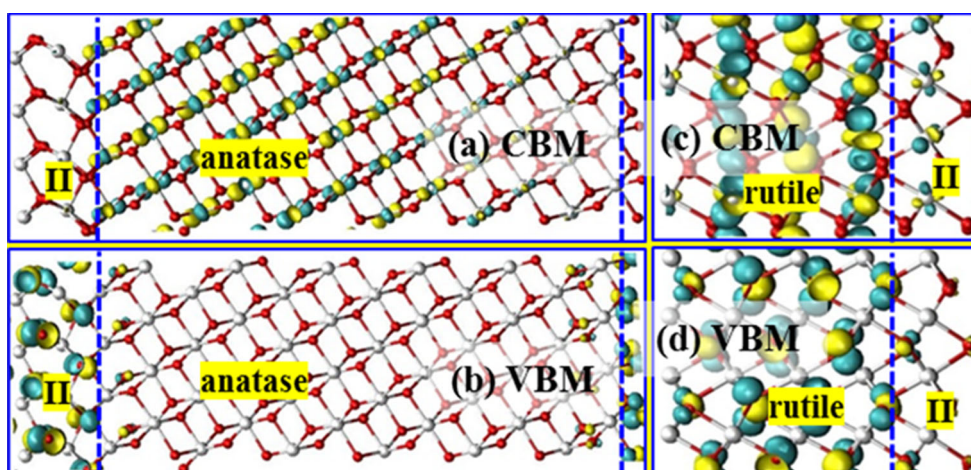
Obviously, there are plenty room to improve the current theoretical methods to treat the phase transition more realistically and to determine the atomic structure in between solids in general.

References

1. Kawahara T, Konishi Y, Tada H, Tohge N, Nishii J, Ito S (2002) Angew Chem 114:2935–2937
2. Scanlon DO, Dunnill CW, Buckeridge J, Shevlin SA, Logsdail AJ, Woodley SM, Catlow CRA, Powell MJ, Palgrave RG, Parkin IP (2013) Nat Mater 12:798–801
3. Kang J, Wu F, Li S-S, Xia J-B, Li J (2012) J Phys Chem C 116:20765–20768
4. Ju MG, Sun GX, Wang JJ, Meng QQ, Liang WZ (2014) ACS Appl Mat Interfaces 6:12885–12892
5. Yu ET, McCaldin JO, McGill TC (1992) Solid State Phys 46:1–146
6. Zhang H, Banfield JF (2005) Chem Mater 17:3421–3425
7. Liu B, Khare A, Aydil ES (2011) ACS Appl Mat Interfaces 3:4444–4450
8. Kuo H-L, Kuo CY, Liu CH, Chao JH, Lin CH (2007) Catal Lett 113:7–12
9. Youngblood WJ, Lee SHA, Maeda K, Mallouk TE (2009) Acc Chem Res 42:1966–1973
10. Chen XB, Shen SH, Guo LJ, Mao SS (2010) Chem Rev 110:6503–6570
11. Hochbaum AI, Yang P (2009) Chem Rev 110:527–546
12. Maeda K, Teramura K, Lu D, Takata T, Saito N, Inoue Y, Domen K (2006) Nature 440:295
13. Zhang J, Xu Q, Feng Z, Li M, Li C (2008) Angew Chem Int Ed 47:1766–1769
14. Yang DJ, Liu HW, Zheng ZF, Yuan Y, Zhao JC, Waclawik ER, Ke XB, Zhu HY (2009) J Am Chem Soc 131:17885–17893
15. Carbone L, Cozzoli PD (2010) Nano Today 5:449–493
16. Casavola M, Buonsanti R, Caputo G, Cozzoli PD (2008) Eur J Inorg Chem 2008:837–854
17. Buonsanti R, Grillo V, Carlino E, Giannini C, Gozzo F, Garcia-Hernandez M, Garcia MA, Cingolani R, Cozzoli PD (2010) J Am Chem Soc 132:2437–2464
18. Buonsanti R, Grillo V, Carlino E, Giannini C, Curri ML, Innocenti C, Sangregorio C, Achterhold K, Parak FG, Agostiano A, Cozzoli PD (2006) J Am Chem Soc 128:16953–16970
19. Lazzarini L, Salviati G, Fabbri F, Zha M, Calestani D, Zappettini A, Sekiguchi T, Dierre B (2009) ACS Nano 3:3158–3164
20. Zhao D, Zhang X, Zeng Q, Dong H, Li J, Cai L, Wang C, Zhou W, Xie S (2013) J Nanosci Nanotechnol 13:1291–1294
21. Kim HG, Kim IH, Park JY, Yoo SJ, Kim JG (2014) J Nucl Mater 451:189–197
22. Boston R, Schnepp Z, Nemoto Y, Sakka Y, Hall SR (2014) Science 344:623–626
23. Nagase T, Anada S, Kobayashi K, Yasuda H, Mori H (2014) Mater Trans 55:451–457
24. Asthana A, Shokuhfar T, Gao Q, Heiden PA, Friedrich C, Yassar RS (2010) Adv Sci Lett 3:557–562
25. Eloirdi R, Lin DHM, Mayer K, Caciuffo R, Fanghanel T (2014) J Mater Sci 49:8436–8443
26. Webster NAS, Gan BK, Livk I (2014) Fuel 137:211–215
27. Xu QA, Zhang J, Feng ZC, Ma Y, Wang X, Li C (2010) Chem Asian J 5:2158–2161
28. Wang X, Du YP, Zhang H, Xu Y, Pan YC, Wu T, Hu HL (2014) Food Control 46:108–114
29. Machon D, McMillan P, Xu B, Dong J (2006) Phys Rev B 73:094125–094133
30. Zhang HZ, Banfield JF (2004) Nano Lett 4:713–718
31. Zhang HZ, Huang F, Gilbert B, Banfield JF (2003) J Phys Chem B 107:13051–13060
32. Naicker PK, Cummings PT, Zhang HZ, Banfield JF (2005) J Phys Chem B 109:15243–15249
33. Xiang HJ, Da Silva JLF, Branz HM, Wei S-H (2009) Phys Rev Lett 103:116101
34. Chua AL-S, Benedek NA, Chen L, Finnis MW, Sutton AP (2010) Nat Mater 9:418–422
35. Galib M, Hanna G (2014) J Phys Chem B 118:5983–5993
36. Junghans C, Perez D, Vogel T (2014) J Chem Theory Comput 10:1843–1847
37. Zheng SH, Pfaendtner J (2014) J Phys Chem C 118:10764–10770
38. Shang C, Liu ZP (2013) J Chem Theory Comput 9:1838–1845
39. Zhang XJ, Shang C, Liu ZP (2013) J Chem Theory Comput 9:3252–3260

40. Shang C, Zhang XJ, Liu ZP (2014) Phys Chem Chem Phys 16:17845–17856
41. Shang C, Liu ZP (2012) J Chem Theory Comput 2215–2222
42. Zhang XJ, Shang C, Liu ZP (2013) J Chem Theory Comput 9:5745–5753
43. Shang C, Liu Z-P (2010) J Chem Theory Comput 6:1136–1144
44. Bowles JS, Mackenzie JK (1954) Acta Metall 2:129–137
45. Mackenzie JK, Bowles JS (1954) Acta Metall 2:138
46. Bansal GK, Heuer AH (1974) Acta Metall 22:409–417
47. Wechsler MS, Lieberman TA (1953) Trans Am Inst Min Engrs 197:1503
48. Wayman CM (1964) *New York:Macmillan Co.* Introduction to the Crystallography of Martensitic Transformations, 76
49. Wayman CM (1972) J Less-Common Met 28:97
50. Xiao XL, Luo CP, Liu JW (2002) Sci China Ser E 45:58
51. Yoshida R, Suzuki Y, Yoshikawa S (2005) J Solid State Chem 178:2179–2185
52. Li W, Liu C, Zhou YX, Bai Y, Feng X, Yang ZH, Lu LH, Lu XH, Chan KY (2008) J Phys Chem C 112:20539–20545
53. Bai Y, Li W, Liu C, Yang ZH, Feng X, Lu XH, Chan KY (2009) J Mater Chem 19:7055–7061
54. Zhou WJ, Gai LG, Hu PG, Cui JJ, Liu XY, Wang DZ, Li GH, Jiang HD, Liu D, Liu H, Wang JY (2011) CrystEngComm 13:6643–6649
55. Zheng ZF, Liu HW, Ye JP, Zhao JC, Waclawik ER, Zhu HY (2010) J Mol Catal A 316:75–82
56. Huang CX, Zhu KR, Qi MY, Zhuang YL, Cheng C (2012) J Phys Chem Solids 73:757–761
57. Brohan L, Verbaere A, Tournoux M, Demazeau G (1982) Mater Res Bull 17:355–361
58. Zhu SC, Xie SH, Liu ZP (2014) J Phys Chem Lett 5:3162–3168
59. Banfield JF, Veblen DR, Smith DJ (1991) Am Miner 76:343–353
60. Penn RL, Banfield JF (1998) Science 281:969–971
61. Linsebigler AL, Lu G, Yates JT (1995) Chem Rev 95:735–758
62. Bickley RI, Gonzalez-Carreno T, Lees JS, Palmisano L, Tilley RJD (1991) J Solid State Chem 92:178–190
63. Ohno T, Sarukawa K, Tokieda K, Matsumura M (2001) J Catal 203:82–86
64. Zhang J, Xu Q, Feng Z, Li M, Li C (2008) Angew Chem Int Edit 47:1766–1769
65. Li YF, Liu ZP, Liu L, Gao W (2010) J Am Chem Soc 132:13008–13015
66. Li YF, Liu ZP (2011) J Am Chem Soc 133:15743–15752
67. Zhang H, Banfield JF (2000) J Phys Chem B 104:3481–3487
68. Gilbert B, Zhang H, Huang F, Finnegan MP, Waychunas GA, Banfield JF (2003) Geochem Trans 4:20–27
69. Zhang HZ, Banfield JF (2000) J Mater Res 15:437–448
70. Gribb AA, Banfield JF (1997) Am Miner 82:717–728
71. Zhang HZ, Banfield JF (1999) Am Miner 84:528–535
72. Zhang J, Li MJ, Feng ZC, Chen J, Li C (2006) J Phys Chem B 110:927–935
73. Zhang J, Xu Q, Li M, Feng Z, Li C (2009) J Phys Chem C 113:1698–1704
74. Chaudhuri J, Ram M, Sarkar B (1994) J Mater Sci 29:3484–3488
75. Napolitano E, Mulas G, Enzo S, Delogu F (2010) Acta Mater 58:3798–3804
76. Begin-Colin S, Girot T, Mocellin A, Le Caër G (1999) Nanostruct Mater 12:195–198
77. BeHgin-Colin S, Girot T, Le CaeKr G, Mocellin A (2000) J Solid State Chem 149:48
78. Dutta H, Sahu P, Pradhan S, De M (2003) Mater Chem Phys 77:153–164
79. Ricci PC, Carbonaro CM, Stagi L, Salis M, Casu A, Enzo S, Delogu F (2013) J Phys Chem C 117:7850–7857
80. Gouma PI, Mills MJ (2001) J Am Ceram Soc 84:619–622
81. Tsukamoto D, Shiraishi Y, Sugano Y, Ichikawa S, Tanaka S, Hirai T (2012) J Am Chem Soc 134:6309–6315
82. Xia T, Li N, Zhang YL, Kruger MB, Murowchick J, Selloni A, Chen XB (2013) ACS Appl Mat Interfaces 5:9883–9890
83. Deskins NA, Kerisit S, Rosso KM, Dupuis M (2007) J Phys Chem C 111:9290–9298
84. Dubrovinskaia NA, Dubrovinsky LS, Ahuja R, Prokopenko VB, Dmitriev V, Weber HP, Osorio-Guillen JM, Johansson B (2001) Phys Rev Lett 87:275501–275504
85. Jeanloz R (1989) J Geophys Res 94:5873–5886
86. Zhao WN, Zhu SC, Li YF, Liu ZP (2015) Chem Sci. doi:10.1039/C5SC00621J